A WAVE-BASED DAMAGE INDEX FOR THE ANALYSIS OF THE FILTERED RESPONSE OF DAMAGED BEAMS

Nicole Apetre, Massimo Ruzzene, Sathyanaraya Hanagud and S. Gopalakrishnan

A WAVE-BASED DAMAGE INDEX FOR THE ANALYSIS OF THE FILTERED RESPONSE OF DAMAGED BEAMS

NICOLE APETRE, MASSIMO RUZZENE, SATHYANARAYA HANAGUD AND S. GOPALAKRISHNAN

This paper introduces a wave propagation-based damage index which relies on the evaluation of the strain energy distribution associated with propagating waves. The presence of localized damages typically distorts the wavefield by causing reflections and diffractions. The evaluation of such distortions, in reference to the wavefield corresponding to the undamaged structure, can be used as an indicator which potentially locates, quantifies and classifies the damage.

The damage index formulation is first illustrated through a numerical model of a beam with a small notch, modeled as a localized thickness reduction. The beam's wave propagation response is simulated through the combined application of perturbation techniques and the spectral finite element method. The perturbation approach and a first order model for the beam capture the coupling between bending and axial behavior caused by the damage, and allow the prediction of mode conversion phenomena. The perturbation solution allows direct comparison between undamaged and damaged strain energy contributions, which are directly associated with perturbation solutions of different orders. The resulting damage index locates the damage along the beam length and estimates its severity.

Experimentally, the damage index is implemented by considering full wavefield measurements obtained through a scanning laser vibrometer. The undamaged reference response is derived directly from measurements on the damaged component, through the application of a filtering procedure operating in the wavenumber/frequency domain.

1. Introduction

The objective of a structural health monitoring (SHM) system is to identify anomalies or damages such as cracks, delaminations, and disbonds in structures. The term identification includes the determination of the existence of damages, their location, and their size as accurately as possible. In the literature, the amount of information that can be obtained regarding a damaged structure is typically classified into five levels: (1) identification of the presence of damage, (2) determination of the location of the damage, (3) classification of the type of damage, (4) quantification of its extent, and (5) estimation of the remaining life of the component under investigation. The definition of an effective measure of damage responds to the requirements of the first 4 stages, and ideally provides inputs to step (5). Damage indices proposed in the literature from an SHM perspective are meant to identify and locate the damage, and, in some cases, to provide an indication regarding the extent of the damage and its progression.

Many SHM techniques developed over the years are based on the detection of changes in the modal behavior of the monitored components. A valuable review of the state-of-the-art in modal-based SHM can be found in [Doebling et al. 1996]. The existing techniques vary on the basis of the type of dynamic response signals used for the analysis, and on the features or parameters considered as damage indicators. Examples include techniques based on changes in modal frequencies [Ostachowicz and Krawczuk 1991; Kim and Stubbs 2003], in measured mode shapes and their spatial derivatives (curvatures) [Pandey et al. 1991; Lestari 2001; Luo and Hanagud 1997; Ho and Ewins 1999], in calculated mean modal strain energies [Sharma et al. 2006; Choi and Stubbs 2004; Cornwell et al. 1999] and in measured flexibility coefficients. Although effective, these methods generally are not sensitive enough to to detect small damages, and often require comparisons with baseline measurements on undamaged specimens. Their lack in sensitivity and their inability to discriminate damage from changes in the operating conditions of modal-based methods can be overcome through the application of guided ultrasonic waves (GUWs) inspections [Staszewski et al. 2004; Rose 2002; Raghavan and Cesnik 2007]. Guided waves, such as Lamb waves, show sensitivity to a variety of damage types and have the ability to travel relatively long distances within the structure under investigation. For this reason, GUWs are particularly suitable for SHM applications, which may employ a built-in sensor/actuator network to interrogate and assess the state of health of the structure [Staszewski et al. 2004; Rose 2002; Giurgiutiu et al. 2003; Giurgiutiu 2005; 2008]. Alternatively, full wavefield measurements can be obtained through scanning laser vibrometers, which allow the implementation of strain energy-based damage index [Sharma et al. 2006], and of frequency/wavenumber filtering techniques for improved damage visualization [Ruzzene 2007]. Interaction of the ultrasonic waves with various scatterers that represent arbitrary thickness variation was study by experimental techniques and was validated with analytical and numerical models such as hybrid boundary element method [Cho and Rose 1996; Cho 2000], finite difference method and finite element method [Kazys et al. 2006; Basri and Chiu 2004], local interaction simulation approach [Ruzzene et al. 2005] and acoustic wavefield imaging [Michaels et al. 2005].

This paper extends the approach in [Ruzzene 2007], by introducing a wave propagation-based damage index which relies on the estimation of the strain energy associated with waves reflected by damage. The approach is illustrated through numerically simulated data which are obtained from the model of a notched beam. The model considers damage as a small, localized thickness reduction, which allows the application of perturbation techniques [Apetre et al. 2008; Lestari 2001]. The resulting perturbation equations are solved in the frequency domain using the spectral finite element method (SFEM) [Doyle 1997; Lee et al. 2000]. SFEM, developed from matrix structural methods [Przemieniecki 1968], is using a discrete Fourier transform to translate a problem to the frequency domain where an exact solution can be found.

In the field of SHM, the SFEM has been previously used for example in [Kumar et al. 2004] to describe the behavior of a first-order shear deformable beam with a transverse crack. Also, the SFE model of a cracked Timoshenko beam is presented in [Krawczuk et al. 2003], where a massless spring, with bending and shear flexibilities computed using Castigliano's theorem and the laws of fracture mechanics is used to model the crack. A review of damage detection using SFEM is presented in [Ostachowicz 2008]. The perturbation approach applied herein leads to a set of linear equations for increasing order of the perturbation parameter. In this context, the separation between the response of the undamaged structure (zero order perturbation solution) and the changes introduced by damage (first order perturbation

solution) is immediate. The proposed damage index formulation is defined as the ratio of the strain energy distribution associated with perturbations due to damage and the strain energy of the undamaged structure, which in the numerical model respectively correspond to the first order and zero order solutions. The formulation can be easily extended for the analysis of full-field experimental data according to procedures outlined in [Ruzzene 2007].

   The paper is organized as follows. Section 2 describes the numerical model of the notched beam, while Section 3 presents the damage index formulation and a set of illustrative numerical examples. The experimental implementation of the concept with the simultaneous application of frequency/wavenumber filtering procedures are presented in Section 4. A summary of the main results of the work is finally presented in Section 5.

2. Wave propagation model for notched beams

Damage description. A detailed derivation of the governing differential equations for a notched Euler-Bernoulli beam is presented in [Apetre et al. 2008]. Here for completeness, a short summary of the derivation is given. The dynamic behavior of the notched beam shown in Figure 1 is described by a set of governing equations derived through the Hamilton principle. The defect is modeled as a reduction in thickness of depth h_d, extending over a length Δl, placed at the distance x_d. As seen in the figure, $x \in [0, L]$ denotes the horizontal coordinate, whereas the vertical coordinate z varies in the interval

$$z \in \left[-\frac{h}{2}, \ \frac{h}{2}(1 - 2\varepsilon\gamma_d(x)) \right], \tag{2-1}$$

where $\varepsilon = h_d/h$, and where $\gamma_d(x) = H(x - (x_d - \Delta l)) - H(x - x_d)$ is a damage function with H denoting the Heaviside function. Both the stiffness and the mass loss due to the edge notch are considered. The moment of inertia at the damage location is truncated at ε order as

$$I_d = I(1 - \varepsilon)^3 \approx I(1 - 3\varepsilon), \tag{2-2}$$

where I is the moment of inertia of the undamaged beam. Thus the expressions for the stiffness and mass distribution along the beam are [Lestari 2001]

$$EI_d(x) = EI[1 - 3\varepsilon\gamma_d(x)] \quad \text{and} \quad m_d(x) = m[1 - \varepsilon\gamma_d(x)], \tag{2-3}$$

where EI and m are the stiffness and the mass of the undamaged beam.
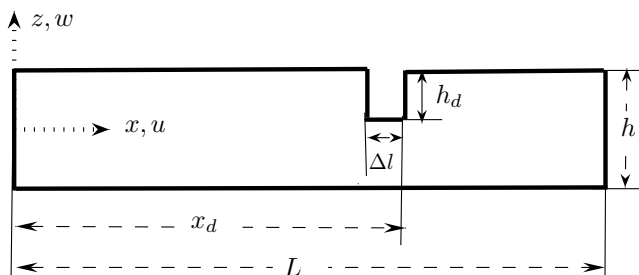
Figure 1. Beam geometry.

Perturbation equations. The governing equations for the notched beam and the appropriate set of boundary conditions are derived using Hamilton's Principle. The required kinetic and strain energies, and the work of external forces are formulated using the first-order approximation

$$u(x, z, t) = u(x, t) - z\frac{\partial w}{\partial x}, \quad w(x, z, t) = w(x, t), \tag{2-4}$$

where $u(x, t)$ and $w(x, t)$ are the axial and transverse displacements in the reference plane $z = 0$, respectively. Application of Hamilton's Principle yields the following set of differential equations:

$$\left[EAu_{,x} + \left(-u_{,x} + w_{,xx}\frac{h}{2}\right)EA\gamma_d(x)\varepsilon\right]_{,x} - m[1 - \varepsilon\gamma_d(x)]\ddot{u} - \frac{mh}{2}\varepsilon\gamma_d(x)\dot{w}_{,xx} = f_1(x, t), \tag{2-5}$$

$$\left[-EIw_{,xx} + \left(-u_{,x} + w_{,xx}\frac{h}{2}\right)E\frac{Ah}{2}\gamma_d(x)\varepsilon\right]_{,xx} + \frac{mh}{2}[\ddot{u}\varepsilon\gamma_d(x)]_{,x} - m[1 - \varepsilon\gamma_d(x)]\ddot{w} = f_2(x, t), \tag{2-6}$$

where E is the Young's modulus, A is the lateral area, h is beam thickness, m is the mass per unit length, and $f_1(x, t)$, $f_2(x, t)$ denote the applied distributed generalized loads, assumed for simplicity to be applied along the reference plane $z = 0$. The important feature of equations (2-5), (2-6) is the coupling between the axial and transverse displacement resulting from the damage description considered. It is noted that in the absence of damage, the small parameter ε becomes zero and equations (2-5), (2-6) reduce to the classical uncoupled equations governing bending and axial behavior of a symmetric beam.

The governing equations can be conveniently expressed in the frequency domain through the application of the Fourier transform, by letting the applied generalized loads $f_j(x, t)$ (with $j = 1, 2$) be

$$f_j(x, t) = \sum_k \hat{f}_{j_k}(x, \omega_k)e^{i\omega_k t}, \tag{2-7}$$

where $i = \sqrt{-1}$, and $\hat{f}_{j_k}(x, \omega_k)$ denotes the harmonic component of the generalized load at frequency ω_k [Doyle 1997]. Accordingly, the beam's axial and transverse displacements can be written as

$$u(x, t) = \sum_k \hat{u}_k(x, \omega_k)e^{i\omega_k t}, \quad w(x, t) = \sum_k \hat{w}_k(x, \omega_k)e^{i\omega_k t}, \tag{2-8}$$

where $\hat{u}_k(x, \omega_k)$, $\hat{w}_k(x, \omega_k)$ are the displacements corresponding to the kth harmonic component. In the remainder of the paper, the subscript k is dropped to simplify notation, so that $\omega_k = \omega$, $\hat{u}_k(x, \omega_k) = \hat{u}(x, \omega)$, $\hat{w}_k(x, \omega) = \hat{w}(x, \omega)$.

Next, the axial and vertical displacements of the beam in the reference plane are expanded as perturbations (in terms of a small parameter ε) of the axial and vertical displacement of the undamaged beam

$$\hat{\mathbf{u}}(x, \omega) = \hat{\mathbf{u}}^{(0)}(x, \omega) - \varepsilon\hat{\mathbf{u}}^{(1)}(x, \omega) - \mathbb{O}(\varepsilon^2), \tag{2-9}$$

where $\hat{\mathbf{u}} = \{\hat{u}\ \hat{w}\}^T$. Substituting (2-8), (2-9) into the differential system (2-5), (2-6) and collecting the coefficients of ε^0 and ε^1 results in the set of differential equations

$$\varepsilon^0 : \mathbf{M}\hat{\mathbf{u}}^{(0)}(x, \omega) + \mathbf{E}_1\hat{\mathbf{u}}_{,xx}^{(0)}(x, \omega) + \mathbf{E}_2\hat{\mathbf{u}}_{,4x}^{(0)}(x, \omega) = \hat{\mathbf{f}}^{(0)}(x, \omega), \tag{2-10}$$

$$\varepsilon^1 : \mathbf{M}\hat{\mathbf{u}}^{(1)}(x, \omega) + \mathbf{E}_1\hat{\mathbf{u}}_{,xx}^{(1)}(x, \omega) + \mathbf{E}_2\hat{\mathbf{u}}_{,4x}^{(1)}(x, \omega) = \hat{\mathbf{f}}^{(1)}(x, \omega), \tag{2-11}$$

where

$$\mathbf{M} = \begin{bmatrix} m\omega^2 & 0 \\ 0 & m\omega^2 \end{bmatrix}, \quad \mathbf{E}_1 = \begin{bmatrix} EA & 0 \\ 0 & 0 \end{bmatrix}, \quad \mathbf{E}_2 = \begin{bmatrix} 0 & 0 \\ 0 & -EI \end{bmatrix}, \tag{2-12}$$

where $A = bh$ and $I = bh^3/12$. In (2-11), $\hat{\mathbf{f}}^{(1)}(x, \omega)$ is the load on the first order perturbation equation, which is a function of the zero order displacement $\hat{\mathbf{u}}^{(0)}$ and is responsible for the axial-bending coupling. Its explicit expression can be found in [Apetre et al. 2008].

Spectral finite element discretization. The equation for the ε^0 term corresponds to the uncoupled governing equation for the undamaged beam in the frequency domain, while the first order perturbation equation has the same form, with an applied generalized load that is a function of $\hat{\mathbf{u}}^{(0)}$. A common strategy for the solution of the equations (2-10), (2-11) is based on their formally identical form. Each of the equations can in fact be written in matrix form as

$$\mathbf{M}\hat{\mathbf{u}}(x, \omega) + \mathbf{E}_1\hat{\mathbf{u}}_{,xx}(x, \omega) + \mathbf{E}_2\hat{\mathbf{u}}_{,4x}(x, \omega) = \mathbf{q}(x, \omega), \tag{2-13}$$

where coefficients are 2×2 matrices. We assume that the beam can be divided into finite elements where an element j of length L_j connects two nodes (Figure 2). The behavior of each node is described by 3 degrees of freedom, so that the element's vector of degrees of freedom is defined as $\mathbf{d}_j = \{\hat{u}_{1j}, \ \hat{w}_{1j}, \ \hat{w}_{1j,x}, \ \hat{u}_{2j}, \ \hat{w}_{2j}, \ \hat{w}_{2j,x}\}^T$. The displacement $\hat{\mathbf{u}}(x, \omega)$ within element j is obtained as an interpolation of the nodal degrees of freedom $\mathbf{d}_j$

$$\hat{\mathbf{u}}(x, \omega) = \mathbf{N}_j(x, \omega)\mathbf{d}_j(\omega), \tag{2-14}$$

where $\mathbf{N}_j(x, \omega)$ is the matrix of dynamic shape functions, which are obtained from the solution of the homogeneous governing equation [Doyle 1997]. The application of the dynamic shape functions as interpolation functions is the main feature of the SFEM, which otherwise maintains the formalism of conventional FEs as demonstrated by the theoretical description of this section. Accordingly, the dynamic shape functions $\mathbf{N}_j(x, \omega)$ provide a description of the displacement variation within an element, which is as exact as the homogeneous distributed parameter model used for the description of the problem at hand [Doyle 1997]. In the case considered here, it can be shown that the generalized load in the first order (ε^1) perturbation equations reduces to a concentrated nodal load if a node is placed at the damage location. Then, the solution of the homogeneous beam equations and the proper description of nodal loads corresponding to the presence of damage based on the formulation presented above can be used to obtain exact dynamic shape functions and accurate representations of the beam's displacements in the frequency range corresponding to the applied load. This approach can also be applied when loads are generally distributed along the element length. In this case the dynamic shape functions do not reproduce exactly the displacement field within the element, and some approximation is introduced. The
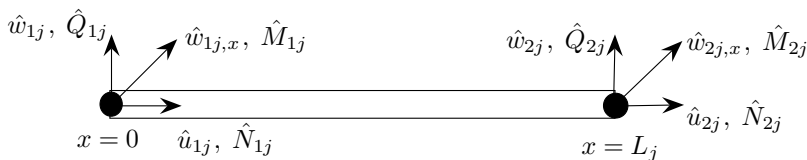
Figure 2. Spectral finite element with nodal displacements and loads.

application of nodes at damage and load locations do not cause a dramatic increase in the computational cost, since only a node needs to be added at each damage and loading site, as opposed to the highly refined meshes that are required for the accurate simulation of wave propagation phenomena with FEs based on the polynomial interpolation of the nodal degrees of freedom. Therefore, the presented modeling approach still represents an efficient tool for the analysis of wave propagation in the considered class of damaged structures. Refinements of the formulation, allowing the accurate representation of general load distributions and of damage locations within the element will be discussed in a forthcoming paper.

Based on the weak formulation of the governing equations (2-13), we can derive the equation

$$\mathbf{K}_j(\omega)\mathbf{d}_j(\omega) = \mathbf{f}_j(\omega), \tag{2-15}$$

where $\mathbf{K}_j(\omega)$ is the element stiffness matrix at frequency ω, defined as

$$\mathbf{K}_j(\omega) = \int_0^{L_j} \left\{ \mathbf{N}_j^T(x, \omega)\mathbf{M}\mathbf{N}_j(x, \omega) - \mathbf{N}_{j,x}^T(x, \omega)\mathbf{E}_1\mathbf{N}_{j,x}(x, \omega) + \mathbf{N}_{j,xx}^T(x, \omega)\mathbf{E}_1\mathbf{N}_{j,xx}(x, \omega) \right\} dx, \tag{2-16}$$

and where $\mathbf{f}_j$ is the vector of applied nodal loads

$$\mathbf{f}_j(\omega) = \int_0^{L_j} \mathbf{N}_j^T(x, \omega)\mathbf{q}(x, \omega)\, dx, \tag{2-17}$$

Numerical results. The numerical model is used to simulate the response of beams with notches, and specifically to illustrate mode conversion phenomena captured by the model considered. The results are obtained by first transforming the time history of the applied load in the frequency domain through the application of the fast Fourier transform (FFT) algorithm. The nodal displacements corresponding to the various harmonic components are then computed through inversion of the dynamic stiffness matrix of the structure according to (2-17). At each frequency, the displacements' variation along the elements' length is obtained through interpolation using the dynamic shape functions (2-14). Final application of the inverse FFT provides the displacements' variation in time.

An aluminum (Young's modulus $E = 70\,\text{GPa}$, density $\rho = 2750\,\text{kg/m}^3$) beam of length $L = 1\,\text{m}$, thickness $h = 1 \times 10^{-2}\,\text{m}$ and width $b = 5 \times 10^{-2}\,\text{m}$ is considered in the simulations. The beam has a notch of length $\Delta l = 1 \times 10^{-2}\,\text{m}$ and depth h_d, located at $x_d = 3L/4$. The beam is modeled using two spectral elements for a total of nine degrees of freedom (Figure 3). The applied load is a longitudinal tip force whose variation in time is described by a Hanning modulated sine burst at $500\,\text{kHz}$ (Figure 4).

Figure 5 shows the variation of the displacements in time and space, while Figure 6 shows snapshots of the beam's deformed configuration at three instants in time. The longitudinal wave generated by the applied load propagates from the tip of the beam and gets partially reflected and converted when it reaches the notch at $x_D = 3L/4$. Mode conversion phenomena such as the one illustrated in this example are
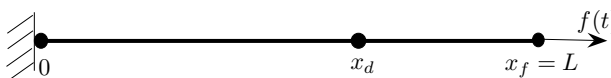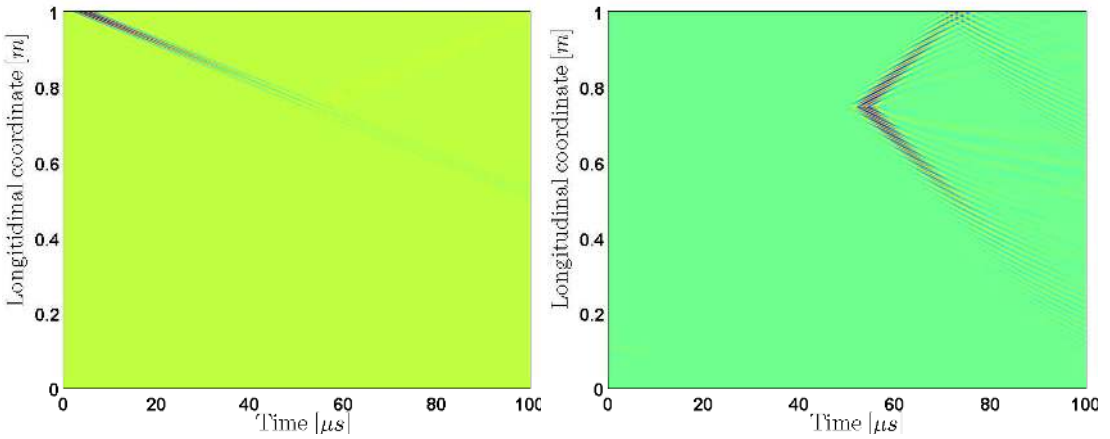

Figure 3. Schematic of the clamped-free beam with a longitudinal tip load, modeled using two spectral elements.
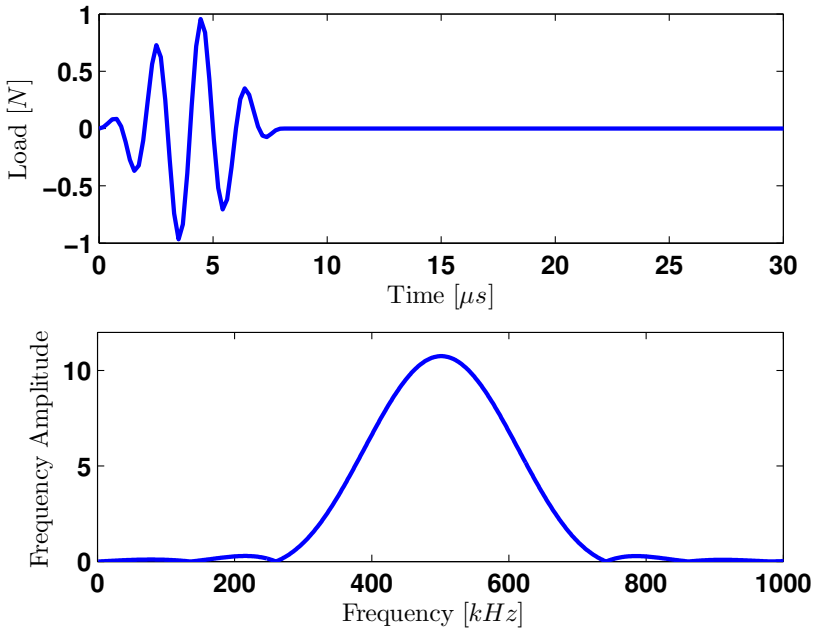
**Figure 4.** Modulated sinusoidal pulse load in time and frequency domain.

Figure 5. Longitudinal (left) and transverse (right) displacement as functions of time and longitudinal coordinate. Notch length $\Delta l = 0.001$ m.

very important as they may be exploited to increase the sensitivity of damage detection and interpretation techniques.

3. Wave-based damage index formulation

Theoretical background. The perturbation analysis is used to define a damage index (DI) which locates the notch and estimates its severity. The definition is such that the DI has value 1 at undamaged locations,
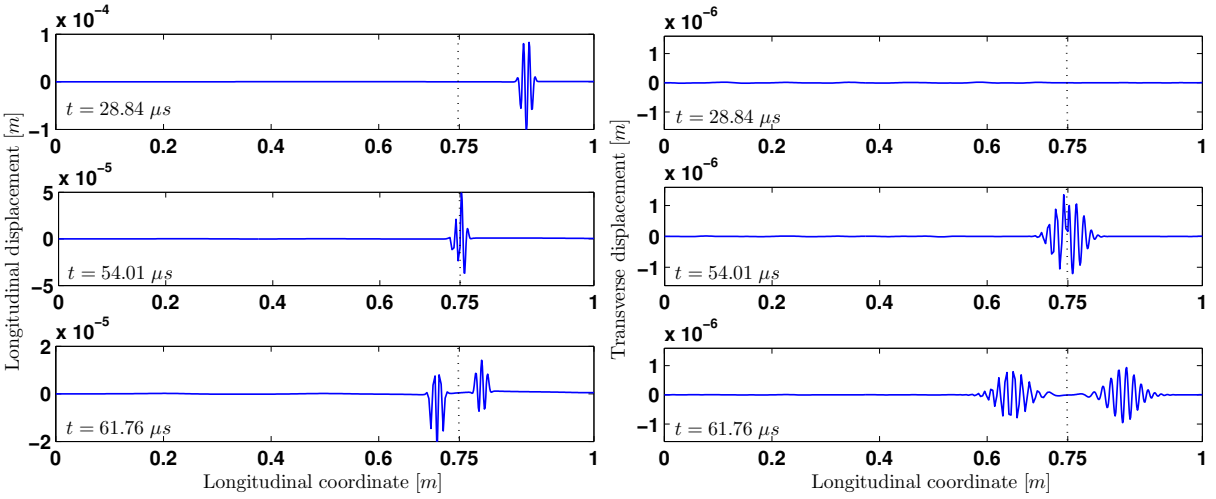
Figure 6. Longitudinal (left) and transversal (right) displacements as function of longitudinal coordinate, for three instants in time.

while it deviates from unity in the vicinity of the notch. The formulation is based on the estimation of the distribution of strain energy associated with propagating and reflected waves. In the proposed approach, which follows procedures previously applied on modal curvature data of notched plates [Sharma et al. 2006], the beam is divided into N segments, over which the strain energy is evaluated through integration over the segment length. At a given instant of time t, the strain energy over segment p, defined by $x \in [x_p, x_{p+1}]$, is obtained by summing contributions from axial and bending deformations

$$\Delta U_p(t) = U(x_{p+1}, t) - U(x_p, t) = \frac{1}{2} \int_{x_p}^{x_{p+1}} \left[EA u_{,x}^2(x, t) + EI w_{,xx}^2(x, t) \right] dx, \tag{3-1}$$

where u and w can be considered as superpositions of the solutions obtained for various orders of the perturbation parameter of (2-9). Substituting the displacement expansions and truncating at the second order yields the following approximate expression for the strain energy of the damaged beam

$$\Delta U_p(t) \approx \Delta U_p^{(0)}(t) - \varepsilon \Delta U_p^{(1)}(t) - O(\varepsilon^2), \tag{3-2}$$

where

$$\Delta U_p^{(0)}(t) = \frac{1}{2} \int_{x_p}^{x_{p+1}} \left[EA[u_{,x}^{(0)}(x, t)]^2 + EI[w_{,xx}^{(0)}(x, t)]^2 \right] dx \tag{3-3}$$

corresponds to the strain energy of the undamaged beam, and where

$$\Delta U_p^{(1)}(t) = \int_{x_p}^{x_{p+1}} \left[EA u_{,x}^{(0)}(x, t) u_{,x}^{(1)}(x, t) + EI w_{,xx}^{(0)}(x, t) w_{,xx}^{(1)}(x, t) \right] dx \tag{3-4}$$

is the contribution due to damage. In preparation for the analysis of experimental data, the integrals are estimated numerically by using a set of spline functions. This leads to continuous strain energy functions $\Delta U^{(0)}(x, t)$ and $\Delta U(x, t)$. Based on (3-4) and the numerical results presented in the previous section, displacement perturbations occur only when waves reach the notch location. Accordingly, the

corresponding strain energy perturbation $\Delta U_p^{(1)}(x, t)$ originates at the damage location, where it reaches its maximum value [Sharma et al. 2006], to progressively decrease in value as the secondary wave produced by the damage propagates away from the damage. The damage index can be thus defined as a ratio between the strain energies associated with the 1st order perturbation, to the strain energy of the undamaged beam, as quantified by the zero order solution

$$d(x, t) = \frac{\Delta U(x, t)}{\Delta U^{(0)}(x, t)} \approx 1 - \varepsilon \frac{\Delta U^{(1)}(x, t)}{\Delta U^{(0)}(x, t)}. \tag{3-5}$$

Equation (3-5) explicitly shows how the deviation from unity of the DI is directly proportional to the perturbation parameter ε which defines the notch depth. The location of damage along the beam length is instead identified by a peak of the $\Delta U^{(1)}(x, t)/\Delta U^{(0)}(x, t)$ function occurring at the damage site.

The above damage index is time-dependent, and it is convenient to consider its cumulative value over a selected time interval

$$d_c(x) = \int_t \left| d(x, t) \right| dt \tag{3-6}$$

to obtain a function depending uniquely on the spatial coordinate.

Numerical examples. Three examples are presented to demonstrate the effectiveness of the proposed damage index formulation as a damage locator and estimator. In all the cases, the beam is simply supported and is excited at a given point by a 5-cycle sinusoidal load. The beam is made of aluminum with Young's modulus $E = 70$ GPa and density $\rho = 2750$ kg/m^3 and has length of $L = 1$ m, thickness $h = 1 \times 10^{-2}$ m and width $b = 5 \times 10^{-2}$ m. The simulation is performed over a time interval which corresponds to the time required for the injected pulse to reach the boundary. The corresponding cumulative DIs are calculated according to (3-6), and plotted in Figure 7. As expected, damage is highlighted by a clear deviation from unity at the damage site. It is important to note how the DI values increase with the notch depth h_D and also shows a monotonic dependence upon the damage width Δl.

The first configuration considers a 5-cycle sinusoidal load applied in the longitudinal direction at $x_f = 0.6L$ and a notch located at $x_f = 0.4L$. According to this load configuration, $w^{(0)} \equiv 0$, and the damage index reduces to

$$d(x, t) = 1 - \varepsilon \frac{\int u_{,x}^{(0)} u_{,x}^{(1)} dx}{\int (u_{,x}^{(0)})^2 dx}. \tag{3-7}$$

Figure 7, top left, shows that for a given notch depth h_D, the DI increases with the damage width Δl.

The results for a transverse load shown in the top right part of the same figure also confirm the damage index behavior. In this last case, the DI can be approximated as

$$d(x, t) = 1 - \varepsilon \frac{\int w_{,xx}^{(0)} w_{,xx}^{(1)} dx}{\int (w_{,xx}^{(0)})^2 dx}, \tag{3-8}$$

since $u^{(0)} \equiv 0$. The graph shows that for a given damage width Δl, the DI increases with the notch depth h_D.

In these two cases, the coupling between longitudinal and transverse displacements due to the damage is of order $\mathbb{O}(\varepsilon^2)$ so it is neglected. To include coupling at $\mathbb{O}(\varepsilon)$, the third configuration considers a 5-cycle sinusoidal load applied in both longitudinal and direction at $x_f = L/2$ and a notch located at $x_f = L/4$.
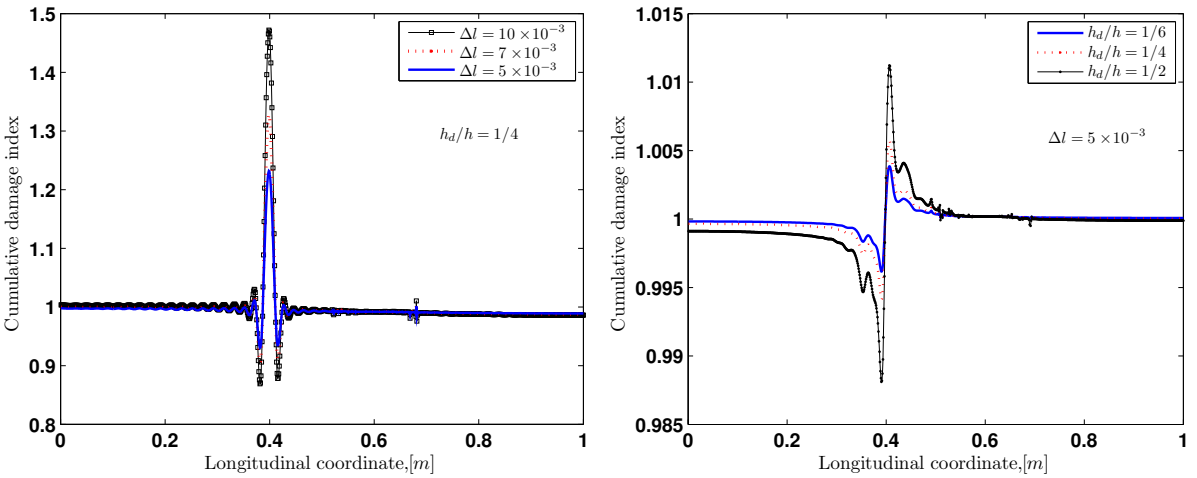
Figure 7. Cumulative damage index results for (left) a horizontal applied load, with $h_d/h = 1/4$ and varying damage length ($\Delta l = 0.005, 0.007, 0.01$ m); and (right) a vertical applied load, with $\Delta l = 0.005$ m and varying damage depth ($h_d/h = 1/6, 1/4, 1/2$).
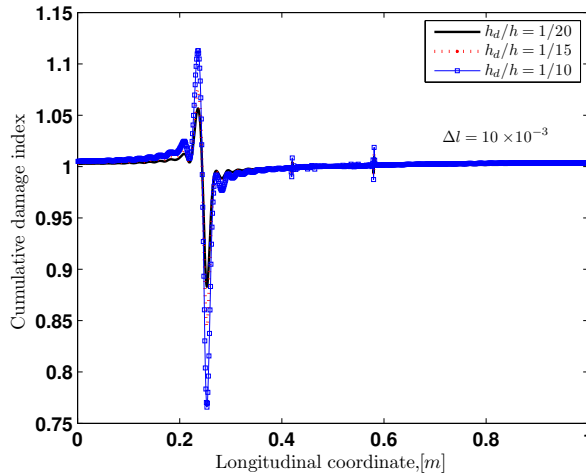
Figure 8. Cumulative damage index results for both horizontal and vertical applied loads, with $\Delta l = 0.01$ m and varying damage depth ($h_d/h = 1/20, 1/15, 1/10$).

Both zero order longitudinal and transverse displacements are present and the DI is given by (3-6). The resulting DI is plotted in Figure 8 for a given damage width Δl and for various notch depths h_D. Once more we see that the DI increases as h_D increases.

4. Experimental implementation

This section presents the extension of the DI concept to the analysis of experimental data. The presented results demonstrate the effectiveness of the DI as a damage indicator, and show its practicality as an inspection tool. The case of a homogeneous plate with a transverse notch is considered. The results in

this section therefore cannot be directly compared with those obtained analytically as the analytical results are obtained for an Euler-Bernoulli beam. Refinements of the analytical formulation to include Lamb modes thus allowing the accurate simulation of the experiments presented here are under development and will be discussed in future papers. However, the objective is to illustrate the application of the concept in a practical setting and to demonstrate how it may be applied to correctly identify the presence of damage.

Experimental evaluation of the DI requires information regarding the undamaged response of the component under investigation and of the perturbation of its response due to the presence of damage. While in the numerical model such information was directly obtained as a by-product of the adopted numerical approach, the effective analysis of experimental data requires the ability to separate these two pieces of information. Preferably, this should be done without need to rely on historical data on the undamaged part. This is here achieved through the application of simple filtering strategies in the wavenumber/frequency domain, which are enabled by the elevated spatial resolution provided by scanning devices such as a scanning laser Doppler vibrometer [Ruzzene 2007]. A summary of this filtering approach, used to remove the reflections due to damage, is presented in the next section, which is followed by the illustration of how the filtering procedure can be used in conjunction with the DI to detect damage in a structure.

Filtering procedure for the estimation of undamaged response. The basic concept behind the filtering technique under consideration is illustrated here for the case of propagating waves in a one-dimensional rod. The data is obtained based on SFE model described in Section 2. Additional details, including the application to two dimensional problems and a more in-depth description can be found in [Ruzzene 2007]. It is assumed that the clamped-free rod is excited at its free end by a modulated harmonic load, which generates a wave. The injected wave interacts with the damage located at $x_d = L/2$, again modeled as a thickness reduction corresponding to $h_d/h = 0.1$, where it is reflected.

The graphs on the left on Figure 9 are snapshots of the rod response at instants of time before, during and after the wave interaction with the notch. After the reflection, the rod's displacement is given by

$$u(x, t) = u^{(i)}(x, t) + u^{(r)}(x, t), \tag{4-1}$$

where one can consider $u^{(i)}(x, t)$ as the 0th order term in the perturbation solution. The two-dimensional FFT in space and time of the rod response is also given by the superposition of contributions from incident and reflected waves

$$\hat{u}(k, \omega) = \hat{u}^{(i)}(k, \omega) + \hat{u}^{(r)}(k, \omega). \tag{4-2}$$

Its representation in the frequency/wavenumber domain shown on the right in Figure 9 highlights the presence of the main pulse propagating along the $x > 0$ direction, and of the reflected pulse propagating in the opposite direction ($x < 0$). As a result, the two corresponding peaks of the two-dimensional FFT appear centered at $\omega = \omega_0$, $k = \pm k_0$. In particular, the reflected pulse has lower amplitude, it is characterized by the same frequency, and appears in the $k > 0$ region of the wavenumber/frequency domain. The two-dimensional representation hence effectively separates incident and reflected wave components. This allows the application of simple filtering strategies, which remove the reflected wave from the recorder signal, thus providing an approximation of the response of the structure in the absence of the damage. For example, a two-dimensional Hanning window can be used to eliminate the reflected
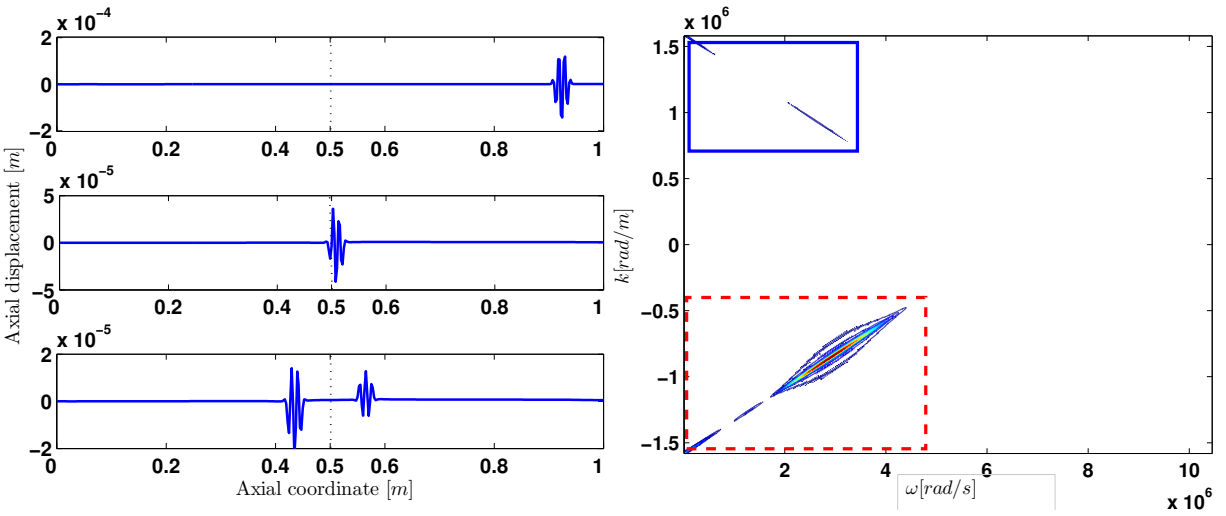
Figure 9. Left: Snapshots of rod deformed configuration at three instants of time. Right: 2D frequency/wavenumber domain representation; the solid box highlights the reflected component, and the dashed box the incident component.

wave and to obtain the frequency/wavenumber spectrum shown in Figure 10, left. Mathematically, the windowing process can be simply expressed as a function product between the wave's two-dimensional FFT and a two-dimensional window function

$$\hat{u}^{(i)}(k, \omega) \approx \left[1 - H(k - k_0, \omega - \omega_0)\right]\hat{u}(k, \omega), \tag{4-3}$$
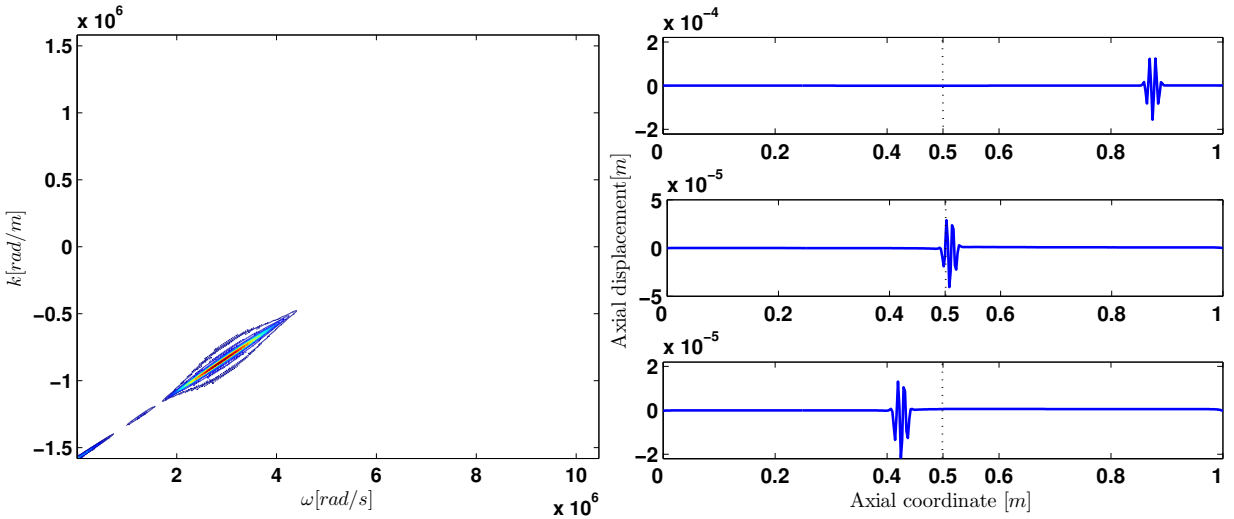

Figure 10. Representation of filtered (incident) axial displacement in the two-dimensional frequency domain (left), and the corresponding deformed configurations at three instants of time (right).
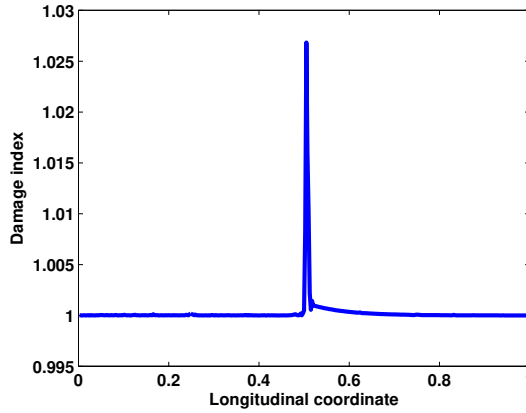
Figure 11. Damage index in a rod.

where $H(k - k_0, \omega - \omega_0)$ denotes the windowing function centered at k_0, ω_0. The incident space-time domain signal can then be reconstructed through inverse Fourier transformation. The incident signal obtained upon filtering at the same instant considered in the left half of Figure 9 is shown in the right half of Figure 10, to demonstrate how the windowing procedure removes the reflected propagating pulse while leaving the response corresponding to the undamaged beam practically unaltered. The separated incident and the total signals can be used for the damage index estimation according to the definition provided above. The result in terms of cumulative damage index for the simple case discussed in this section is plotted in Figure 11.

Experimental set-up for wavefield measurements. A schematic of the set-up is shown in Figure 12. The experimental results are obtained using piezoceramic discs as actuators and a scanning laser Doppler
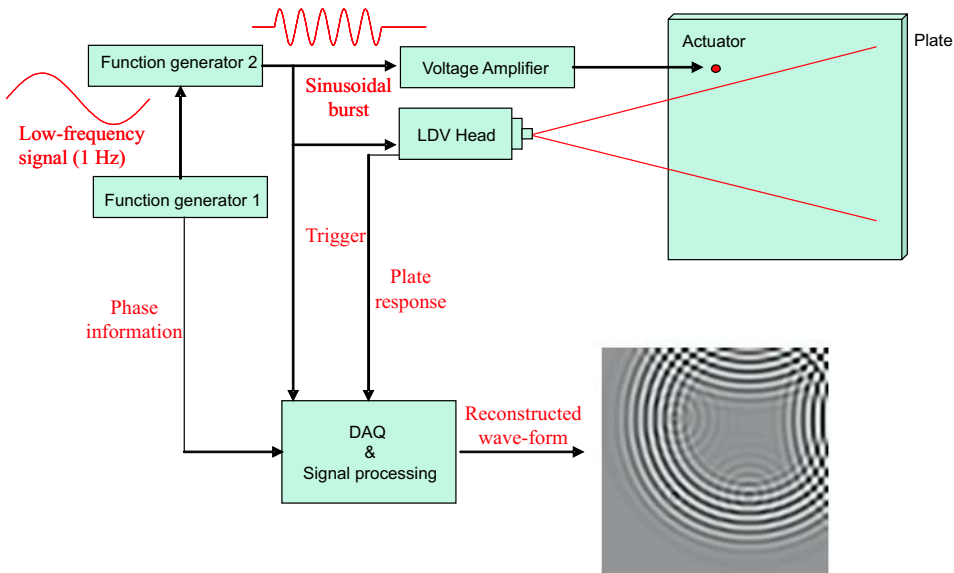

Figure 12. Schematic of experimental set-up for wavefield measurement.

vibrometer (SLDV) as a sensor. The SLDV (Polytec PI, Model PSV400M2) allows frequency sampling up to 1 MHz, which enables GUWs detection and visualization. In the wave propagation tests, the piezodiscs are driven by a sinusoidal burst generated by a signal generator. The resulting elastic waves are recorded at the measurement grid points defined on the scanning system. The operation of the SLDV requires the generation of a pulse at each grid point in order to record the corresponding response. Phase information is retained by triggering the excitation signal through a low frequency signal (10 Hz), which also defines the scanning rate. Upon completion of measurements at all grid points, the recorded responses are postprocessed to obtain full images of the propagating wavefield within the region of inspection.

Shown on the right is a detail top view of a typical test specimen: in this case, an aluminum plate of dimensions $0.76 \, \text{m} \times 0.76 \, \text{m} \times 3.05 \times 10^{-3} \, \text{m}$. The damage is a $27 \times 10^{-3} \, \text{m}$ long and $1 \times 10^{-3} \, \text{m}$ deep grove which was cut in the plate at the location shown. The figure also shows a typical line of measurement points (in the case presented below the number of points is 69). The wave is generated by a surface bonded piezotransducer excited by a 5-cycle, 110 kHz sinusoidal pulse. The responses at the grid points is recorded, stored, and converted for postprocessing. In particular, the responses are interpolated using spline functions, which can be conveniently differentiated for strain energy evaluation.
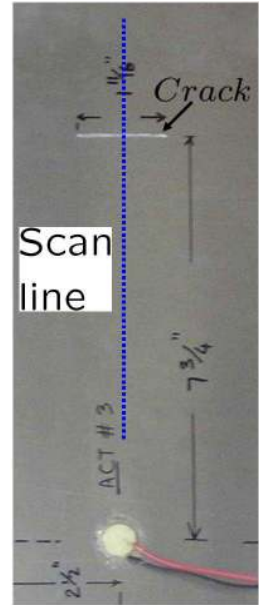
Experimental results. The time-spatial variation of the plate response shows the presence of a low amplitude S_0 mode, which propagates faster than the A_0 mode (Figure 13). The significant difference in amplitude recorded for the two modes is related to their polarization (S_0 is mostly in-plane, while A_0 is mostly out-of-plane) and to the limitation of the currently available SLDV which only measures out-of-plane displacement or velocity components. When the S_0 mode reaches the crack location, it is partially converted into A_0, as well as reflected and transmitted. The detailed spatial information obtained
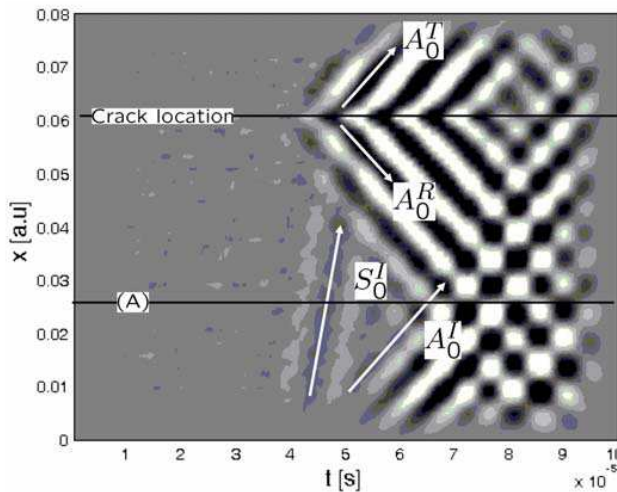
Figure 13. Space-time variation of recorded response showing multimodal wave propagation, mode conversion and reflection at crack location.
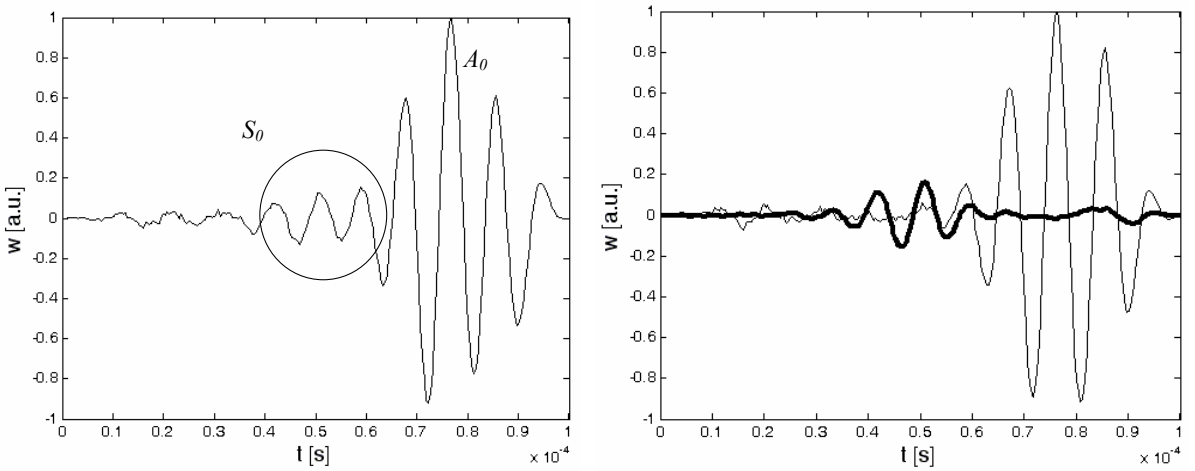
Figure 14. Left: Response at location A of Figure 13. Right: Filtered S_0 response (thick line) and reflected A_0 mode (thin line).

from the SLDV can be used to effectively separate the S_0 mode from the A_0 mode through filtering in the frequency/wavenumber domain. Proper design of the filtering window allows in fact the separation of incident and reflected waves as well as the decoupling of different modes propagating at the same frequency. Figure 14, left shows the time response recorded at location A, while the right half of the same figure compares the two reconstructed signals corresponding to the S_0 mode and the reflected A_0 mode.

Figure 15 shows the variation of the plate incident and reflected responses in time and space as colormap plots. Both responses contain both S_0 and A_0 modes.
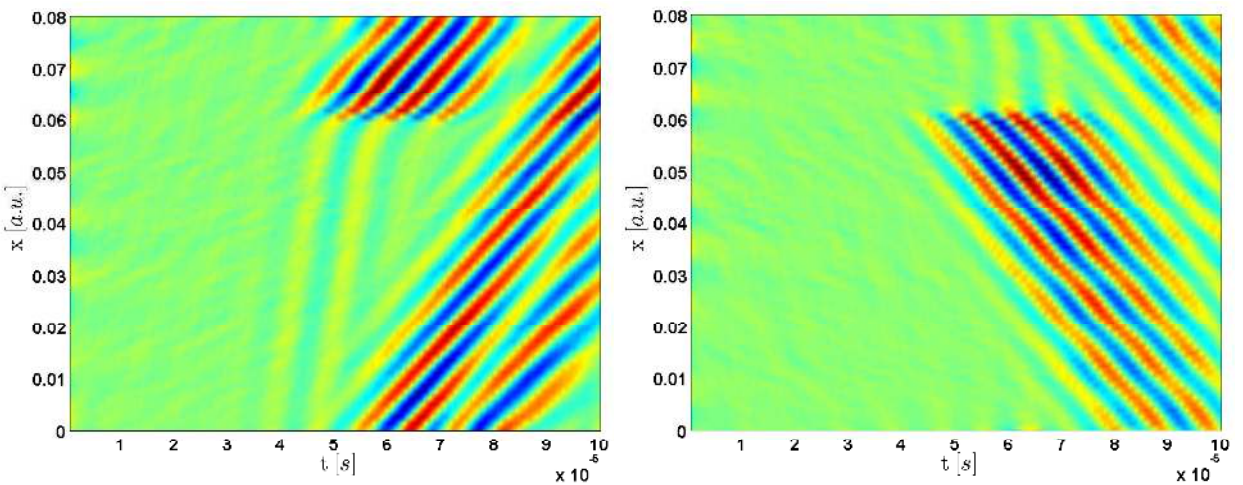
Figure 15. Filtered incident (left) and reflected (right) response as function of time and longitudinal coordinate.
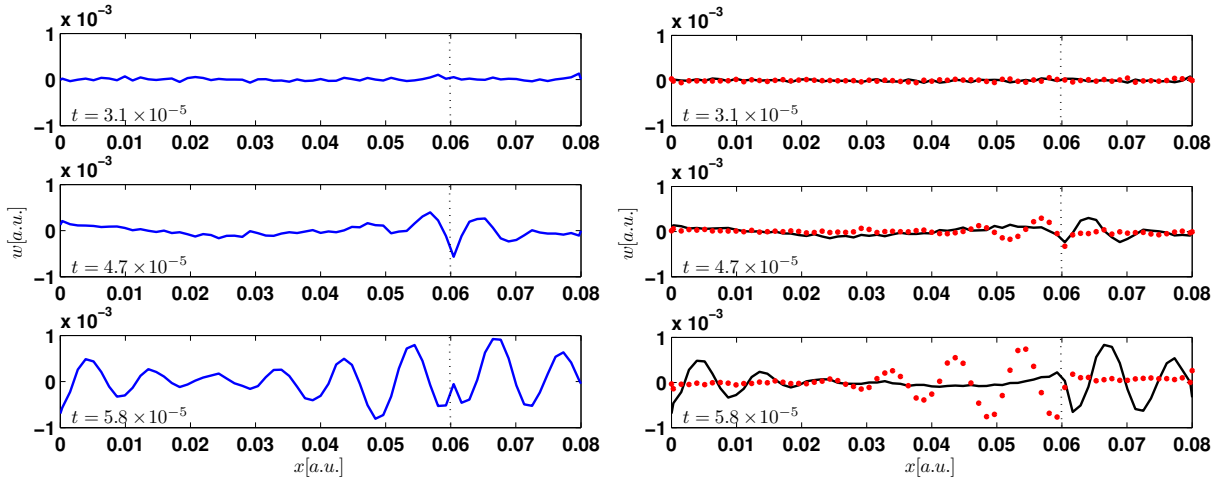
Figure 16. Left: Raw test data (transverse displacement) as function of longitudinal co-
ordinate at three instants. Right: Filtered incident (dotted line) and reflected (continuous
line) waves as function of longitudinal coordinate at the same three moments.

Figure 16 shows snapshots of the displacements' variation along the beam at three instants of time as
raw data and also as filtered data. A very clear separation between the incident and the reflected waves
is presented in Figure 16, right.

Analytically the damage index was defined as the ratio of strain energies associated with damaged
and undamaged beams. Due to the mode conversion phenomena, the damage index obtained from the
experimental data is defined as the ratio of strain energies associated with the damaged beam and with
the incident S_0 mode denoted by S_0^I (Figure 14, left)

$$d(x,t) = \frac{\Delta U(x,t)}{\Delta U^{(S_0^I)}(x,t)}, \tag{4-4}$$

where the stain energy associated with S_0^I is defined as

$$\Delta U^{(S_0^I)}(x,t) = \int \left[w_{,xx}^{(S_0^I)}(x,t)\right]^2 dx \tag{4-5}$$

and where $w^{(S_0^I)}$ is the displacement associated with the S_0^I. As in the analytically defined damage
measure of (3-6), a cumulative damage index is considered and the result is plotted in Figure 17. Due
to the significant difference in amplitude recorded for the two modes the ratio $d(x,t)$ gives very large
values. But the ratio still has a peak at the location of the damage (Figure 17). Refinements of the
proposed DI will be further investigated and in future papers.

5. Conclusions and future work

This paper presents a wave-based damage index and illustrates the model by applying it to both analytical
and experimental data. The formulation is first supported by a numerical method which simulates the
effects of a notch damage on a propagating elastic wave. The numerical technique combines the SFEM
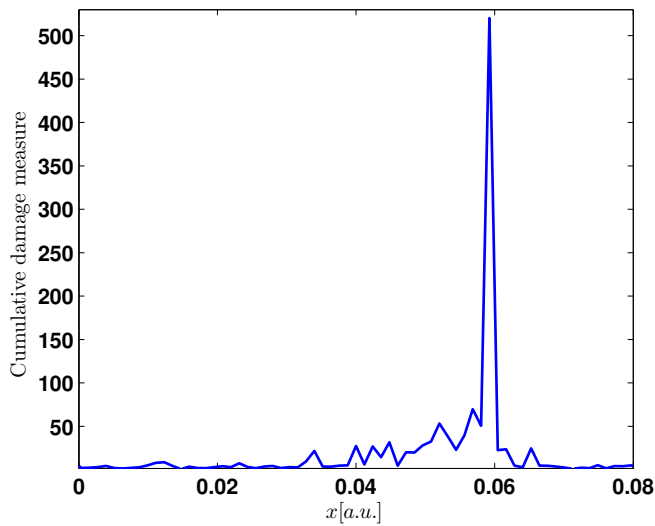
Figure 17. Cumulative damage index of experimental data.

and perturbation techniques and allows the prediction of reflections and mode conversion phenomena associated with wave/damage interactions.

The damage index formulation is based on the distribution of strain energy within the structure. The technique is implemented by estimating the undamaged response through a filtering process that operates in the frequency/wavenumber domain to separate wave components propagating in opposite directions. Numerical results, based on the developed numerical model, as well as experimental data, obtained through a scanning laser vibrometer show the effectiveness of the proposed formulation and its potentials for implementation as a practical inspection tool for detection of the damage location. Future work will include results for the quantification of the damage that are missing in the current development. Also a similar concept will be developed for the case of multimodal signals.

The objective of the paper is to illustrate the effectiveness of the damage index for both analytical and experimental data. The experimental data cannot be validated with the present numerical model, due to the model's limitation to describe higher Lamb modes. Future work includes extensions of the analytical formulation, allowing accurate simulation of the experiments.

Future work will also extend the concept to practical aerospace structures in the presence of structural features such as holes, rivets, or localized impedance changes which complicate the wavefield and its interpretation, and make the identification of the presence of damage much more challenging. The authors are already successful in applying the same tool for two dimensional data in the presence of multiple scatterers. In future work, the authors will demonstrate how multiple scatterers contributions to the scattered field can be resolved to obtain the characterization of the individual scatterers.

References

[Apetre et al. 2008] N. Apetre, M. Ruzzene, S. Hanagud, and S. Gopalakrishnan, "Spectral and perturbation analysis of first-order beams with notch damage", *J. Appl. Mech.* (*ASME*) **75**:3 (2008), 031019.

[Basri and Chiu 2004] R. Basri and W. K. Chiu, "Numerical analysis on the interaction of guided Lamb waves with a local elastic stiffness reduction in quasi-isotropic composite plate structures", *Compos. Struct.* **66**:1–4 (2004), 87–99.

[Cho 2000] Y. Cho, "Estimation of ultrasonic guided wave mode conversion in a plate with thickness variation", *IEEE Trans. Ultrason. Ferroelectr. Freq. Control* **47**:3 (2000), 591–603.

[Cho and Rose 1996] Y. Cho and J. L. Rose, "A boundary element solution for a mode conversion study on the edge reflection of Lamb waves", *J. Acoust. Soc. Am.* **99**:4 (1996), 2097–2109.

[Choi and Stubbs 2004] S. Choi and N. Stubbs, "Damage identification in structures using the time-domain response", *J. Sound Vib.* **275**:3–5 (2004), 577–590.

[Cornwell et al. 1999] P. Cornwell, S. W. Doebling, and C. R. Farrar, "Application of the strain energy damage detection method to plate-like structures", *J. Sound Vib.* **224**:2 (1999), 359–374.

[Doebling et al. 1996] S. W. Doebling, C. R. Farrar, M. B. Prime, and D. W. Shevitz, "Damage identification and health monitoring of structural and mechanical systems from changes in their vibration characteristics: a literature review", Technical report LA-13070-MS, Los Alamos National Laboratory, 1996, Available at http://www.lanl.gov/projects/ei/shm/pubs/lit_review.pdf.

[Doyle 1997] J. F. Doyle, *Wave propagation in structures: spectral analysis using fast discrete Fourier transforms*, 2nd ed., Springer, New York, 1997.

[Giurgiutiu 2005] V. Giurgiutiu, "Tuned Lamb wave excitation and detection with piezoelectric wafer active sensor of structural health monitoring", *J. Intell. Mater. Syst. Struct.* **16**:4 (2005), 291–305.

[Giurgiutiu 2008] V. Giurgiutiu, *Structural health monitoring with piezoelectric wafer active sensors*, Academic Press, Amsterdam, 2008.

[Giurgiutiu et al. 2003] V. Giurgiutiu, J. Bao, and W. Zhao, "Piezoelectric wafer active sensor embedded ultrasonics in beams and plates", *Exp. Mech.* **43**:4 (2003), 428–449.

[Ho and Ewins 1999] Y. K. Ho and D. J. Ewins, "Numerical evaluation of the damage index", pp. 995–1011 in *Structural health monitoring 2000* (Stanford, CA, 1999), edited by F.-K. Chang, Technomic, Lancaster, PA, 1999.

[Kazys et al. 2006] R. Kazys, L. Mazeika, R. Barauskas, R. Raisutis, V. Cicenas, and A. Demcenko, "3D analysis of interaction of Lamb waves with defects in loaded steel plates", *Ultrasonics* **44**:Supplement 1 (2006), e1127–e1130.

[Kim and Stubbs 2003] J. T. Kim and N. Stubbs, "Crack detection in beam type structures using frequency data", *J. Sound Vib.* **259**:1 (2003), 146–160.

[Krawczuk et al. 2003] M. Krawczuk, M. Palacz, and M. Ostachowicz, "The dynamic analysis of a cracked Timoshenko beam by the spectral element method", *J. Sound Vib.* **264**:5 (2003), 1139–1153.

[Kumar et al. 2004] D. S. Kumar, D. R. Mahapatra, and S. Gopalakrishnan, "A spectral finite element for wave propagation and structural diagnostic analysis of composite beam with transverse crack", *Finite Elem. Anal. Des.* **40**:13–14 (2004), 1729–1751.

[Lee et al. 2000] U. Lee, J. Kim, and A. Y. T. Leung, "The spectral element method in structural dynamics", *Shock Vib. Digest* **32**:6 (2000), 451–465.

[Lestari 2001] W. Lestari, *Damage of composite structures: detection technique, dynamic response and residual strength*, Ph.D. thesis, Georgia Institute of Technology, 2001.

[Luo and Hanagud 1997] H. Luo and S. Hanagud, "An integral equation for changes in the structural dynamics characteristics of damaged stuctures", *Int. J. Solids Struct.* **34**:35-36 (1997), 4557–4579.

[Michaels et al. 2005] T. E. Michaels, J. E. Michaels, B. Mi, and M. Ruzzene, "Damage detection in plate structures using sparse transducer arrays and acoustic wavefield imaging", pp. 938–945 in *Review of progress in quantitative nondestructive evaluation*, vol. 24A, edited by D. O. Thompson and D. E. Chimenti, American Institute of Physics, Melville, NY, 2005.

[Ostachowicz 2008] M. Ostachowicz, "Damage detection of structures using spectral finite element method", *Comput. Struct.* **86**:3–5 (2008), 454–462.

[Ostachowicz and Krawczuk 1991] M. Ostachowicz and M. Krawczuk, "Analysis of the effect of cracks on the natural frequencies of a cantilever beam", *J. Sound Vib.* **150**:2 (1991), 191–201.

[Pandey et al. 1991] A. K. Pandey, M. Biswas, and M. M. Samman, "Damage detection from changes in curvature mode shapes", *J. Sound Vib.* **145**:2 (1991), 321–332.

[Przemieniecki 1968] J. S. Przemieniecki, *Theory of matrix structural analysis*, McGraw-Hill, New York, 1968.

[Raghavan and Cesnik 2007] A. Raghavan and C. E. S. Cesnik, "Review of guided-wave structural health monitoring", *Shock Vib. Digest* **39**:2 (2007), 91–114.

[Rose 2002] J. L. Rose, "A baseline and vision of ultrasonic guided wave inspection potential", *J. Pressure Vessel Technol. (ASME)* **124**:3 (2002), 273–282.

[Ruzzene 2007] M. Ruzzene, "Frequency-wavenumber domain filtering for improved damage visualization", *Smart Mater. Struct.* **16** (2007), 2116–2129.

[Ruzzene et al. 2005] M. Ruzzene, S. M. Jeong, T. E. Michaels, J. E. Michaels, and B. Mi, "Simulation and measurement of ultrasonic waves in elastic plates using laser vibrometry", pp. 172–179 in *Review of progress in quantitative nondestructive evaluation*, vol. 24A, edited by D. O. Thompson and D. E. Chimenti, American Institute of Physics, Melville, NY, 2005.

[Sharma et al. 2006] V. Sharma, M. Ruzzene, and S. Hanagud, "Damage index estimation in beams and plates using laser vibrometry", *AIAA J.* **44**:4 (2006), 919–923.

[Staszewski et al. 2004] W. J. Staszewski, C. Boller, and G. Tomlinson (editors), *Health monitoring of aerospace structures: smart sensor technologies and signal processing*, Wiley, West Sussex, 2004.

NICOLE APETRE: nicole.apetre@gatech.edu
School of Aerospace Engineering, Georgia Institute of Technology, 270 Ferst Drive, Atlanta, GA 30332, United States

MASSIMO RUZZENE: ruzzene@ae.gatech.edu
School of Aerospace Engineering, Georgia Institute of Technology, 270 Ferst Drive, Atlanta, GA 30332, United States
http://www.ae.gatech.edu/people/mruzzene/

SATHYANARAYA HANAGUD: hanagud@aerospace.gatech.edu
School of Aerospace Engineering, Georgia Institute of Technology, 270 Ferst Drive, Atlanta, GA 30332, United States

S. GOPALAKRISHNAN: krishnan@aero.iisc.ernet.in
Department of Aerospace Engineering, Indian Institute of Science, Bangalore, 560012, India
http://www.aero.iisc.ernet.in/~krishnan